New Journal of Physics
The open-access journal for physics

Strength through structure: visualization and local assessment of the trabecular bone structure

C Räth[1,7], R Monetti[1], J Bauer[1,2], I Sidorenko[1], D Müller[2], M Matsuura[3], E-M Lochmüller[4], P Zysset[5] and F Eckstein[6]

[1] Max-Planck Institut für Extraterrestrische Physik, Giessenbachstrasse 1, 85748 Garching, Germany
[2] Department of Radiology, Technische Universität München, Klinikum rechts der Isar, Ismaninger Strasse 22, 81675 Munich, Germany
[3] Institute of Anatomy, Ludwig Maximilians Universität München, Pettenkoferstrasse 11, 80336 München, Germany
[4] Department of Gynaecology I, Ludwig Maximilians Universität München, Maistrasse 11, 80337 München, Germany
[5] Institute for Lightweight Design and Structural Biomechanics, Vienna University of Technology (TU-Wien), Gusshausstrasse 27–29, 1040 Wien, Austria
[6] Paracelsus Medical University Salzburg, Strubergasse 21, 5020 Salzburg, Austria
E-mail: cwr@mpe.mpg.de

New Journal of Physics **10** (2008) 125010 (18pp)
Received 29 May 2008
Published 1 December 2008
Online at http://www.njp.org/
doi:10.1088/1367-2630/10/12/125010

Abstract. The visualization and subsequent assessment of the inner human bone structures play an important role for better understanding the disease- or drug-induced changes of bone in the context of osteoporosis giving prospect for better predictions of bone strength and thus of the fracture risk of osteoporotic patients. In this work, we show how the complex trabecular bone structure can be visualized using μCT imaging techniques at an isotropic resolution of 26 μm. We quantify these structures by calculating global and local topological and morphological measures, namely Minkowski functionals (MFs) and utilizing the (an-)isotropic scaling index method (SIM) and by deriving suitable texture measures based on MF and SIM. Using a sample of 151 specimens taken from human vertebrae *in vitro*, we correlate the texture measures with the mechanically measured maximum compressive strength

[7] Author to whom any correspondence should be addressed.

(MCS), which quantifies the strength of the bone probe, by using Pearson's correlation coefficient. The structure parameters derived from the local measures yield good correlations with the bone strength as measured in mechanical tests. We investigate whether the performance of the texture measures depends on the MCS value by selecting different subsamples according to MCS. Considering the whole sample the results for the newly defined parameters are better than those obtained for the standard global histomorphometric parameters except for bone volume/total volume (BV/TV). If a subsample consisting only of weak bones is analysed, the local structural analysis leads to similar and even better correlations with MCS as compared to BV/TV. Thus, the MF and SIM yield additional information about the stability of the bone especially in the case of weak bones, which corroborates the hypothesis that the bone structure (and not only its mineral mass) constitutes an important component of bone stability.

Contents

1. Introduction

Osteoporosis, which is considered as one of the ten most important diseases in the world population, is nowadays defined as a skeletal disorder characterized by compromised bone strength predisposing to an increased risk of fracture [1]. Since this definition appears fairly abstract the following statements were added: bone strength reflects the integration of two main features: bone density and bone quality. Bone density is expressed as grams of mineral per area or volume and in any given individual is determined by peak bone mass and amount of bone loss. Bone quality refers to architecture, turnover, damage accumulation (e.g. microfractures) and mineralization. The measurement of the bone mineral density (BMD) is a well-established technique in the diagnosis of osteoporosis. Evaluating the bone mass with BMD using dual-energy x-ray absorptiometry (DXA) or quantitative computed tomography (QCT) may, however, be insufficient to fully assess the biomechanical strength of the trabecular bone or the fracture risk [2]. Another important component responsible for bone strength is the architecture of the inner bone, the so-called trabecular bone structure, which is not yet assessed as a standard procedure.

An indispensable prerequisite for a quantitative assessment of the trabecular bone structure is a proper three-dimensional (3D) visualization of the complex inner bone network, in which the rod- and plate-like constituents enclosing the bone marrow have a size of the order of 50–200 μm. Advances in tomographic imaging techniques, such as computed tomography (CT), micro CT (μCT) and high-resolution magnetic resonance imaging (HR-MRI) have significantly improved the spatial resolution being now of the order of the trabeculae in bone. Therefore, it has become possible to visualize the complex inner network of the bone structure *in vitro* as well as *in vivo* [3]–[5].

In order to quantitatively characterize trabecular bone structures, it is necessary to use statistical measures which are sensitive to all the essential information about bone structure as presented in 3D tomographic images. There is a variety of conceivable statistical measures which might be used to analyse bone structures. Conventional approaches rely on the use of histomorphometric measures, which are already known from histology [4, 6].

The visual impression of the trabecular structure clearly indicates a complex network—very much like the largest existing structures, namely the (evolved) distribution of galaxies in the Universe with its clusters, filaments and huge voids. Thus, one might be led to the conjecture that also in this case the use of linear measures (power spectrum and autocorrelation function) is not sufficient for a proper description and must rather be complemented with nonlinear measures being sensitive to the higher order spatial correlations (HOC) in the image. In fact, it has been shown using the method of surrogates that the trabecular structure as displayed in 3D HRMRI of osteoporotic and non-osteoporotic bones have nonlinear spatial correlations [7].

Beside these purely statistical reasons (bio-)physical considerations can also lead one to a better motivated choice of statistical description. The architecture of the trabecular bone is the result of continuous bone remodelling which is a complex process involving the resorption of bone on a particular surface followed by a phase of bone formation. In healthy adults, there is a balance between the amount of bone resorbed by osteoclasts and the amount of bone formed by osteoblasts. The bone formation is triggered by external mechanical forces, thus being strain-dependent (see, e.g. [8]–[11] and references therein). In this context not only the strength of the external stimuli matters but also its direction so that the resulting network consists of some aligned structures along the main directions of the forces acting on the bone [12].

These bio-physical mechanisms under the action of external stimuli can also be regarded as a self-organized optimization process, where the resulting trabecular bone structure fulfils the requirements for optimal load transfer by pairing suitable strength and stiffness to minimal weight according to the rules of mathematical design [13].

In this paper, we show that a proper 3D visualization of the trabecular structure is feasible using μCT imaging techniques, which allows for a detailed local structural analysis. To this end we employ global and local Minkowski functionals (MFs) (see, e.g. [14] and references therein) as a class of measures quantifying topological aspects of the bone network. Furthermore, we represent the image data as a 3D point distribution and estimate the local scaling properties using isotropic and anisotropic scaling indices. The scaling index method (SIM) (see, e.g. [15, 16] and references therein) is well suited to quantifying geometrical aspects of the bone structures on a local level, especially to discriminate between (aligned) plate- and rod-like structural elements. The contribution of the various structural features identified using MF and SIM to the strength of the bone specimens is assessed by correlating the newly calculated texture measures with the maximum compressive strength (MCS), which is measured by mechanical testing. We especially investigate whether an additional sophisticated structural analysis yields

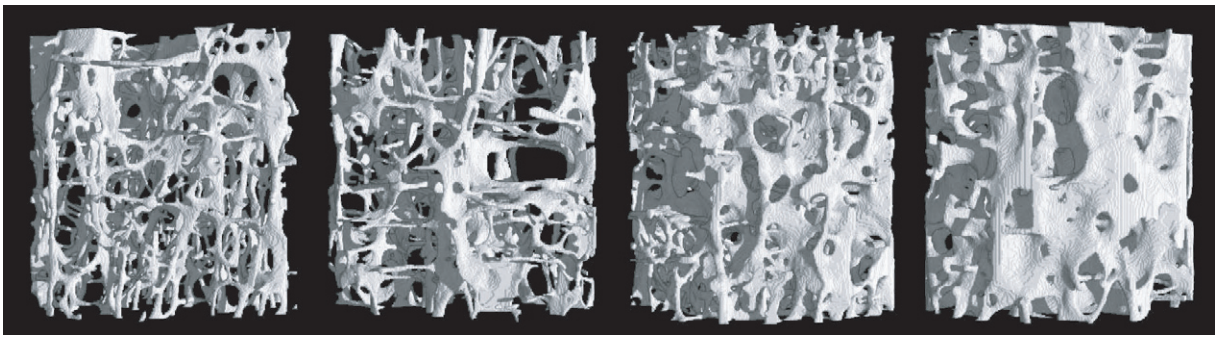

Figure 1. Reconstruction of bone microstructures from μCT scans for four selected specimens with different MCS and/or bone volume/total volume (BV/TV). From left to right: MCS = 17.87 and BV/TV = 0.07; MCS = 82.53 and BV/TV = 0.07; MCS = 90.84 and BV/TV = 0.17; MCS = 157.00 and BV/TV = 0.17.

more information about the bone stability as compared with the mere measurement of the bone volume (BV), and if so, how this is achieved.

The outline of the paper is as follows: in section 2, we describe the preparation of the data set for this study and how the imaging and the mechanical testing of the probes was performed. Section 3 reviews the formalism of the MF and SIM and shows some specific extensions. Our results are presented in section 4. We conclude with section 5 and give a brief outlook to future work.

2. The data set

2.1. μCT imaging

One hundred and fifty one cylindrical specimens were harvested from spines (73 thoracic vertebrae and 78 lumbar vertebrae) using diamond trephines (Salzmann, Munich, Germany) as described previously [4], with an 8 mm inner diameter drill. The sample is heterogeneous, i.e. bones harvested from 58 men and 54 women cadavers were considered. The mean age of the donors was 80 ± 10 years. The donors had agreed to dedicate their body to the institute several years prior to death. The length of the probes was set to 14 mm. The samples were stored in a solution of 5% buffered formalin until μCT scanning. The scans were acquired for the central 6 mm in length of the specimen using a μCT 20 scanner (Scanco Medical, Brütisellen, Switzerland). The resolution was set to 26 μm (isotropic), similar to a previous study on human trabecular bone [4]. In that system, a microfocus x-ray tube with a focal spot of 10 μm is used as a source. The filtered 40 kVp x-ray spectrum is peaked at 25 keV allowing excellent bone versus soft tissue contrast owing to the pronounced photoelectric effect. The integration time was 100 ms leading to a total scan time of 4.1 h per sample. The grey-value images were segmented using a low-pass filter by convolving the image with a Gaussian kernel with a standard deviation of 0.8 and a support of 1 to remove noise and a fixed global threshold equal to 22% of maximal grey value to extract the mineralized bone phase. These binarized 3D images as shown in figure 1 represent the basis of all subsequent image postprocessing steps.

2.2. Mechanical testing

After μCT measurements, the bone samples were cut to a length of 12 mm with parallel surfaces using a saw microtome (Leica Microsystems Inc, Wetzlar, Germany). The bone marrow was removed by washing and ultrasonic cleaning (Sonorex, Bandelin electronic, Berlin, Germany). Bone samples were embedded in polymethylmethacrylate (Beracryl, Bauer HandlesGmbH, Adetswil, Switzerland) to a depth of 1.5 mm on each end. The embedded samples were tested using a servohydraulic testing machine (MTS 858 mini Bionix II, MTS Eden Prairie, USA) with a load cell of 1.5 kN. After 12 preconditioning cycles to 0.35% of strain at a speed of 0.005 mm s^{-1}, the samples were loaded to 6% compressive strain at the same velocity of 0.005 mm s^{-1}. Force and displacement were recorded for the last two cycles and the final loading up to the strain of 6%. Ultimate strength was identified from the largest stress value of the force-displacement curve. MCS was calculated from this first local maximum of the stress–strain curve.

3. Trabecular bone structure analysis

3.1. Histomorphometric measures

The traditional way for assessing the structural properties of cancellous bone is the calculation of the four so-called histomorphometric measures (i) BV/TV, (ii) trabecular number (Tr.N), (iii) trabecular thickness (Tr.Th) and (iv) trabecular separation (Tr.Sp). These four quantities were computed in 3D as described previously [4]. In addition, the structure model index (SMI) [17]—a global measure of plate- or rod-like trabecular architecture—and the bone surface (BS) were calculated using the analysis software delivered by the μCT-manufacturer. It is worth noticing that the BV fraction and the BS find exact correspondences in two of the four global MFs described below.

3.2. MFs

The characterization of the morphology of spatial patterns is relevant in different branches of science. In order to investigate the geometry and topology of typical structural motifs, it is necessary to use objective quantitative measures. The MFs are a set of scalar measures suitable for the description of the morphology of structures (for a review about MF and its applications in morphological image processing see [14]). The usefulness of these functionals has already been demonstrated in the analysis of galaxy catalogues and simulations of large scale structure [18]–[24], as well as of the temperature distribution in maps of the cosmic microwave background radiation [25]–[28]. Furthermore, they were also used to characterize the morphology of spinodal decomposition [29] and of patterns arising in reaction–diffusion systems [30].

MFs are defined only for convex bodies. In fact, convex bodies play a relevant role in integral geometry. A collection of points K in the d-dimensional Euclidean space is called a convex set if for every pair of points in K, the entire line segment joining them lies in K as well. A convex set with non-empty interior is called a convex body. We will restrict our attention to compact sets, i.e. convex sets that are bounded and closed. If a parallel body K_ϵ is considered, i.e. the set that contains all points closer to K than $\epsilon > 0$, and if K is convex, then the general

expression for the volume V of the parallel body K_ϵ at a distance ϵ is given by the Steiner formula [31, 32]

$$V(K_\epsilon) = \sum_{\nu=0}^{d} \binom{d}{\nu} W_\nu^{(d)}(K)\epsilon^\nu, \tag{1}$$

where the $W_\nu^{(d)}(K)$ are called *quermassintegrals* or MFs and are given by

$$W_0^{(1)}(K) = l(K), \quad W_1^{(1)}(K) = 2, \quad d = 1, \tag{2}$$

$$W_0^{(2)}(K) = A(K), \quad W_1^{(2)}(K) = \tfrac{1}{2}U(K), \quad W_2^{(2)}(K) = \pi, \quad d = 2, \tag{3}$$

$$W_0^{(3)}(K) = V(K), \quad W_1^{(3)}(K) = \tfrac{1}{3}S(K), \quad W_2^{(3)}(K) = \frac{2\pi}{3}B(K),$$
$$W_3^{(3)}(K) = \frac{4\pi}{3}, \quad d = 3, \tag{4}$$

where $l(K)$, $A(K)$, $U(K)$, $V(K)$, $S(K)$ and $B(K)$ denote the length, the area, the boundary length, the volume, the surface and the mean breadth, respectively. It should be mentioned that parallel sets keep the properties of convexity and compactness. The MFs have very important properties (like motion invariance, C-additiveness and continuity) whose discussion is beyond the scope of this work. It is worth mentioning, however, a fundamental result in integral geometry about the completeness of the family of the MF. A theorem by Hadwiger [33] states that every motion invariant, C-additive and continuous functional ϕ over K can be written as

$$\phi(K) = \sum_{\nu=0}^{d} a_\nu W_\nu^{(d)}(K), \tag{5}$$

where $a_\nu \in \mathbb{R}$. Thus, the $d+1$ MF forms a complete system of morphological measures on the set of convex bodies. The use of MF to characterize the morphology of images requires further consideration. In order to allow for the application of MF to images, it is necessary to introduce the concept of a convex ring [33]. A convex ring $\mathcal{R}$ is the class of all subsets $A \in \mathbb{R}^d$ which can be expressed as finite unions of compact convex sets

$$A = \bigcup_{i=1}^{l} K_i, \quad K_i \in \mathbb{K}. \tag{6}$$

If A_1, $A_2 \in \mathcal{R}$ then $A_1 \bigcup A_2 \in \mathcal{R}$ and $A_1 \bigcap A_2 \in \mathcal{R}$. Given an additive functional ϕ then $\phi(A_1 \bigcup A_2) = \phi(A_1) + \phi(A_2) - \phi(A_1 \bigcap A_2)$. Motion invariance of ϕ on $\mathcal{R}$ is derived from motion invariance for ϕ on $\mathbb{K}$. It should be noted that a binary image is an instance of the convex ring $\mathcal{R}$, where the black pixels are the convex sets, i.e. the elements of $\mathbb{K}$.

The Euler characteristic or connectivity number χ is an important functional which allows us to extend the application of MF from K to $\mathcal{R}$ and thus to images. It is defined as [33]

$$\chi(K) = \begin{cases} 1, & K \neq \emptyset, \\ 0, & K = \emptyset, \end{cases} \tag{7}$$

for all $K \in \mathbb{K}$. The Euler characteristic is an additive, motion invariant functional on $\mathcal{R}$. In $d = 2$, χ is given by the number of connected components minus the number of holes. For $d = 3$,

χ can be obtained as the number of connected components minus the number of tunnels plus the number of cavities.

As mentioned above, each pixel of a 2D or 3D image is a convex set. Therefore, such an image may be considered as an element of the convex ring $\mathcal{R}$ and thus one can build additive image functionals to characterize the image morphology. However, some care has to be taken because MFs are only defined on convex sets. The key to the practical application of integral geometry to images is the additivity of χ. Further details of the derivation are beyond the scope of this paper. The interested reader is referred to [14]. For a 2D binary image, it can be shown that all MFs can be calculated by assuming that pixels are squares with linear size normalized to one. Then, the procedure to evaluate the three MFs consists of two steps. First, every black pixel is decomposed into four vertices, four edges and the interior of a pixel. Then the total number of squares n_s, edges n_e and vertices n_v are counted to evaluate the area M_1, perimeter M_2 and Euler characteristic M_3 from

$$M_1 = n_s, \quad M_2 = -4n_s + 2n_e, \quad M_3 = n_s - n_e + n_v. \tag{8}$$

The procedure to calculate MF for 3D binary images is analogous to the one in 2D with the only difference that each black pixel is now the union of eight vertices, 12 edges, six faces and the interior of the cube. The four MFs, namely the volume M_1, the surface area M_2, the mean breadth M_3 and the Euler characteristic M_4, are defined as

$$M_1 = n_c, \quad M_2 = -6n_c + 2n_f \quad 2M_3 = 3n_c - 2n_f + n_e \quad M_4 = -n_c + n_f - n_e + n_v, \tag{9}$$

where n_c and n_f are the number of cubes and faces, respectively.

In this paper, we calculate MF in 3D to characterize the morphology of μCT tomographic images of the human spine. In order to compute the MF, it is necessary to binarize the images. Previous application of the MF to MRI and CT images of human trabecular bone by Böhm *et al* [34, 35] focused on the characterization of the contribution to the image structure of different grey-level regions using global functionals. These studies were carried out using a moving threshold procedure to binarize the grey-level distribution of the tomographic image. Thus, the behaviour of the global MF as a function of the grey-level value is obtained. As mentioned above, μCT images have a standardized grey-level distribution which allows us to easily obtain the 3D mineral network by thresholding the distribution. A visual inspection of the mineral network reveals (see figure 1) that it is far from being homogeneous but is highly complex, i.e. it contains regions with high density volumes and plates, low density rods, different orientations, etc. After generating a binary image, one can evaluate global and local MFs. Local MF can be applied to investigate the scaling behaviour of the different functionals. In this paper, we compute local MF to account for the diversity of local structural components. However, the local MF were only evaluated for a typical scale of the trabecular network, namely for the mean trabecular spacing ($\sim$1.2 mm). Using this scale, we expect to obtain an optimal contrast between MF values for the different substructures (rods, plates, dense regions, etc). For the sake of comparison, global MFs were also calculated. Cubes of side approximately the mean trabecular spacing were considered to evaluate the local MF. The local values of the MF were compiled into a probability density (P_{M_i}) which provides the frequency of the different substructures that compose the mineral network. For instance, the probability density for the volume (first MF) tells us how heterogeneous the bone density is (see figure 2).

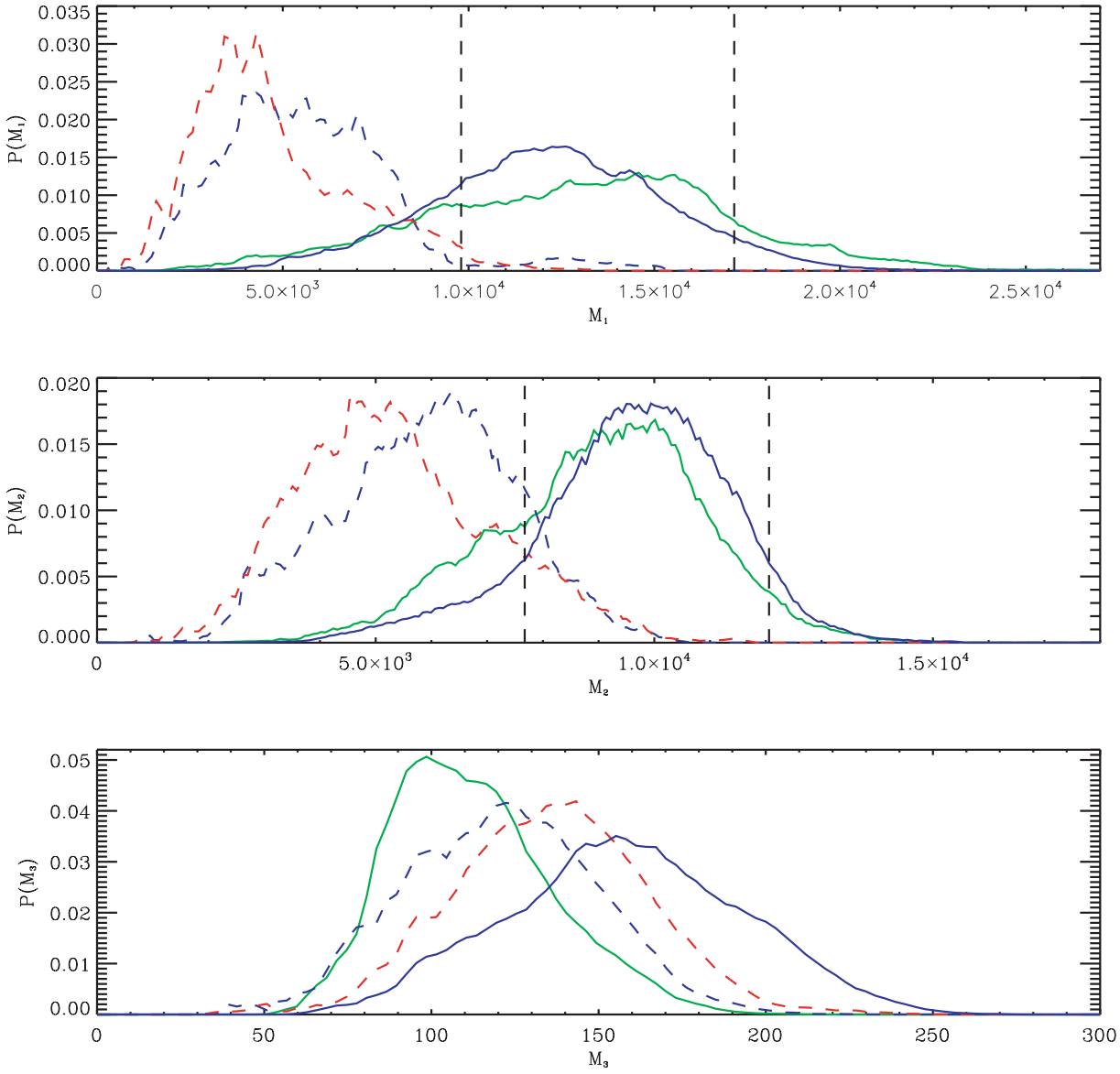

Figure 2. Probability distributions of the local MFs for the four selected specimens. From top to bottom: volume M_1, surface area M_2 and mean breadth M_3. Green solid line: MCS = 157.00, BV/TV = 0.17, blue solid line: MCS = 90.84, BV/TV = 0.17, blue dashed line: MCS = 82.53, BV/TV = 0.07 and red dashed line: MCS = 17.87, BV/TV = 0.07. The black dashed vertical lines indicate the window positions for the texture measures $\Delta P(M_1)$ and $\Delta P(M_2)$.

3.3. Isotropic and anisotropic weighted scaling indices

The weighted SIM offers a possibility to estimate the local isotropic and anisotropic scaling properties of a point set, which is generally represented in a d-dimensional space. From this knowledge it is possible to infer information about the local structural elements of the point set. The basic ideas of the method stem from the characterization of strange attractors in a phase space representation of dissipative dynamical systems which exhibit chaotic behaviour using

correlation dimension [36] and crowding indices [37, 38]. Beside the countless applications of these measures in the realm of nonlinear time series analysis, it has also been demonstrated that this approach can successfully be used for texture analyses in 2D and 3D image data [5, 39, 40]. Let us review the formalism for 3D image data.

The first step of the SIM is to create a set of n-dimensional vectors. For time series this is most often done using the method of delay coordinates ([41] and references therein). Images can just as well be represented as point distributions in an artificial embedding space by comprising the spatial and intensity information of each pixel in a d-dimensional vector. Since we consider in this study only binarized 3D images, a suitable representation of the image information as a set of 3D vectors is given by $\vec{p}_i = (x_i, y_i, z_i), i = 1, \ldots, N_{\text{bones}}$, where N_{bones} denotes the number of bone voxels and x_i, y_i, z_i, the voxel positions.

For each point the local weighted cumulative point distribution ρ is calculated. In general form this can be written as

$$\rho(\vec{p}_i, r) = \sum_{j=1}^{N} s_r(d(\vec{p}_i, \vec{p}_j)), \tag{10}$$

where $s_r(\bullet)$ denotes a kernel function depending on the scale parameter r and $d(\bullet)$ a distance measure.

The weighted scaling indices $\alpha(\vec{p}_i, r)$ are obtained by calculating the logarithmic derivative of $\rho(\vec{p}_i, r)$ with respect to r,

$$\alpha(\vec{p}_i, r) = \frac{\partial \log \rho(\vec{p}_i, r)}{\partial \log r} = \frac{r}{\rho}\frac{\partial}{\partial r}\rho(\vec{p}_i, r). \tag{11}$$

In principle, any differentiable kernel function and any distance measure can be used for calculating α. For the case of isotropic scaling indices, we use the Euclidean norm $\| \bullet \|_2$ as a distance measure and a set of Gaussian shaping functions. So the expression for ρ simplifies to

$$\rho(\vec{p}_i, r) = \sum_{j=1}^{N} \mathrm{e}^{-((d_{ij}/r))^q}, \quad d_{ij} = \| \vec{p}_i - \vec{p}_j \|_2 \ . \tag{12}$$

The exponent q controls the weighting of the points according to their distance to the point for which α is calculated. The higher q is chosen the more steplike becomes the weighting function resembling more and more the Heaviside-function, which is used for the calculation of the unweighted scaling indices. Another interesting choice of q is given by $q = 2$. In this case, the kernel function is the well-known Gaussian exponential function.

Throughout this study we calculate α for the case $q = 2$. Inserting equation (12) in the definition for the weighted scaling indices (equation (11)) yields the following analytical expression for α:

$$\alpha(\vec{p}_i, r) = \frac{\sum_{j=1}^{N} q((d_{ij}/r))^q \mathrm{e}^{-((d_{ij}/r))^q}}{\sum_{j=1}^{N} \mathrm{e}^{-((d_{ij}/r))^q}}. \tag{13}$$

Structural components of a point set are characterized by the value of α. For example, points in a point-like structure have $\alpha \approx 0$ and voxels forming rod-like structures have $\alpha \approx 1$. Sheet-like structures are characterized by $\alpha \approx 2$ of the voxels belonging to them. A uniform distribution of points yields $\alpha \approx d$ which is equal to the dimension of the configuration space.

Table 1. Correlation coefficients r between MCS and the histomorphometric parameters, SMI, BS, M_3 and M_4 calculated for the whole sample. Note that BV/TV $\simeq M_1$ and BS $\simeq M_2$.

BV/TV	Tr.N	Tr.Th	Tr.Sp	SMI	BS	M_3	M_4
0.73	0.43	0.30	−0.41	−0.43	0.61	0.06	−0.38

Anisotropic scaling indices are calculated by using a generalized quadratic distance measure $\| \bullet \|_{\mathbf{A}}$, where $\mathbf{A}$ is a metric tensor. In the general case $\mathbf{A}$ ($\mathbf{A} = \mathbf{R}^{\mathbf{T}} \cdot \mathbf{M} \cdot \mathbf{R}$) is a product of a rotation matrix $\mathbf{R}$ and a diagonal matrix $\mathbf{M}$ containing the eigenvalues λ_x^2, λ_y^2 and λ_z^2. In this study, in which the known direction of the external force is assumed to induce a globally constant preferential direction, namely the z-direction, we only calculate anisotropic scaling indices parallel and perpendicular to this direction, i.e. along the three major axes x, y and z [42]. By only considering these three anisotropic scaling indices α_x, α_y, α_z, and thus omitting rotations depending on arbitrary values of the rotation angles ϕ and θ, the calculation of the respective distances d_{ij} is considerably simplified and only depends on the choice of the eigenvalues λ_x^2, λ_y^2 and λ_z^2,

$$d_{ij}(\lambda_x, \lambda_y, \lambda_z) = \left(\lambda_x^2(x_i - x_j)^2 + \lambda_y^2(y_i - y_j)^2 + \lambda_z^2(z_i - z_j)^2\right)^{1/2} . \tag{14}$$

We chose the ratio 5 : 1 for the eigenvalues, i.e. $5\lambda_x = \lambda_y = \lambda_z$ (and respective permutations), for setting the degree of anisotropy along the three directions. This setting was found to be well suited especially for the detection of aligned cylindrical structures (i.e. the trabeculae) with typical mean breadth and length.

As for the local MFs we compile the isotropic and anisotropic scaling indices for the point set in a frequency distribution $N(\alpha)$

$$N(\alpha)\mathrm{d}\alpha = \#(\alpha \in [\alpha, \alpha + \mathrm{d}\alpha]) \tag{15}$$

or equivalently in the probability distribution

$$P(\alpha)\mathrm{d}\alpha = \mathrm{Prob}(\alpha \in [\alpha, \alpha + \mathrm{d}\alpha]). \tag{16}$$

The $P(\alpha)$-representation of a point set can be regarded as a structural decomposition of the data where the points are differentiated according to the local isotropic and anisotropic morphological features of the structure elements to which they belong.

4. Results

To correlate the texture measures with the mechanical strength of the bone specimens we use Pearson's correlation coefficient r. The r values obtained for the standard histomorphometric measures are summarized in table 1.

We find strong correlations for BV/TV and also for BS, whereas the other histomorphometric measures, namely Tr.N, Tr.Th, Tr.Sp, the SMI and the third and fourth MFs gave no or only moderate correlations with MCS. Therefore, only the global measures BV/TV and BS will be considered in our more detailed, load-dependent analyses, which will be described in the following.

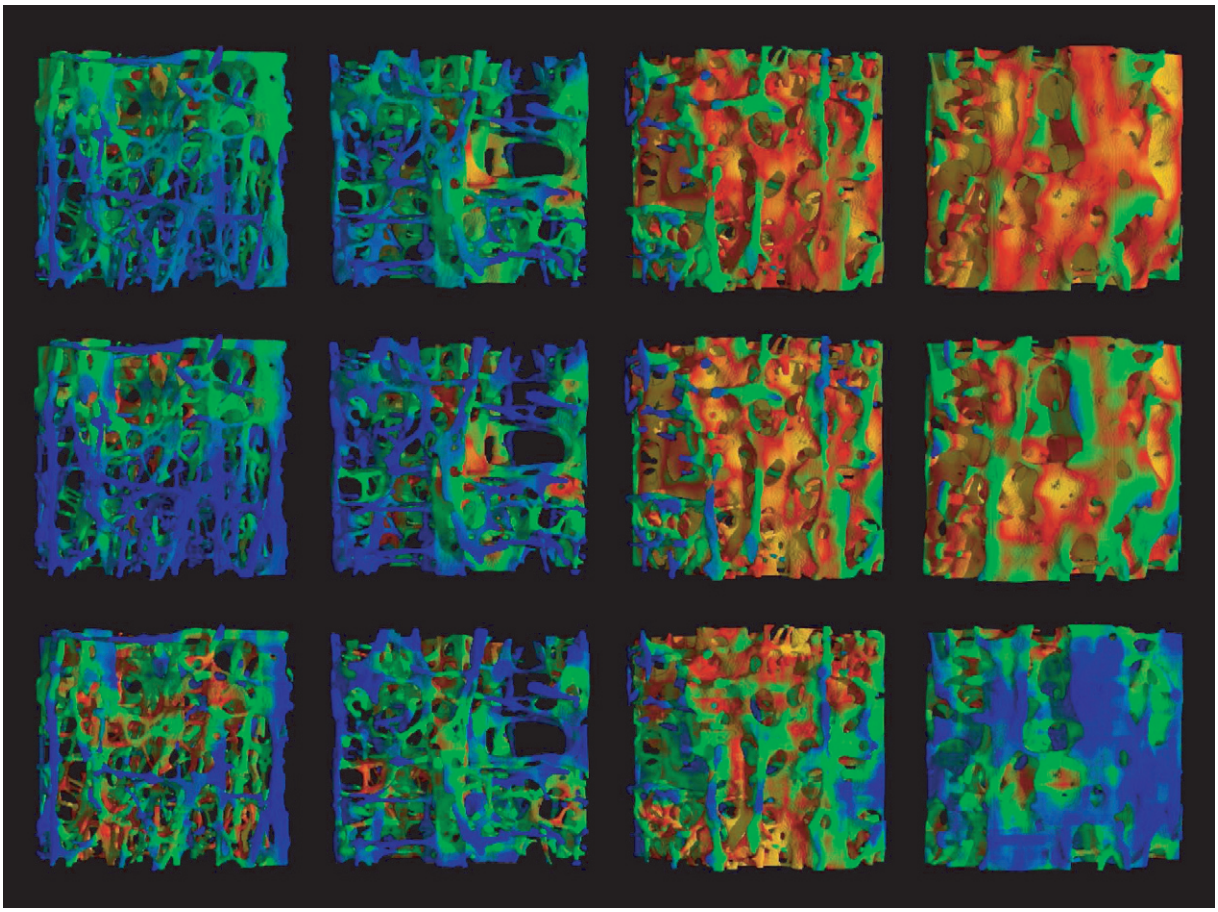

Figure 3. Colour-coded visualization of the local MFs for the images shown in figure 1. Upper row: volume M_1, middle row: surface area M_2 and lower row: mean breadth M_3. (See stacks.iop.org/NJP/10/125010/mmedia for animations of selected images.)

In figure 2, the probability distribution of the local MFs for the four selected specimens are displayed. Figure 3 shows the corresponding colour-coded 3D visualization. From figure 2 one clearly sees that the distribution for the local volume M_1 shows the expected shift towards smaller values for weaker bones. A similar behaviour is observed for the BS M_2, whereas M_3 does not show such a clear systematic trend. This is then also reflected in poor results for the correlations with MCS, which we have not included in the text. It should be noted that the probability distribution for the local Euler characteristic M_4 turned out to be rather discrete with only a few different values and did not show any discriminative power. Therefore, this measure is not included in the analyses either.

Figures 4 and 5 show the respective probability densities and visualization for the scaling indices. The spectra for the isotropic scaling index α also show the expected shift towards lower values for weaker bones indicating the transition from more predominant plate-like structural elements in healthy bone to rod-like structures in rarefied osteoporotic bone. The spectra for the two anisotropic scaling indices α_x and α_y are qualitatively very similar with a peak at $\alpha_{x,y} \approx 2.1$ and a larger tail towards higher values. A quite different shape can be observed for

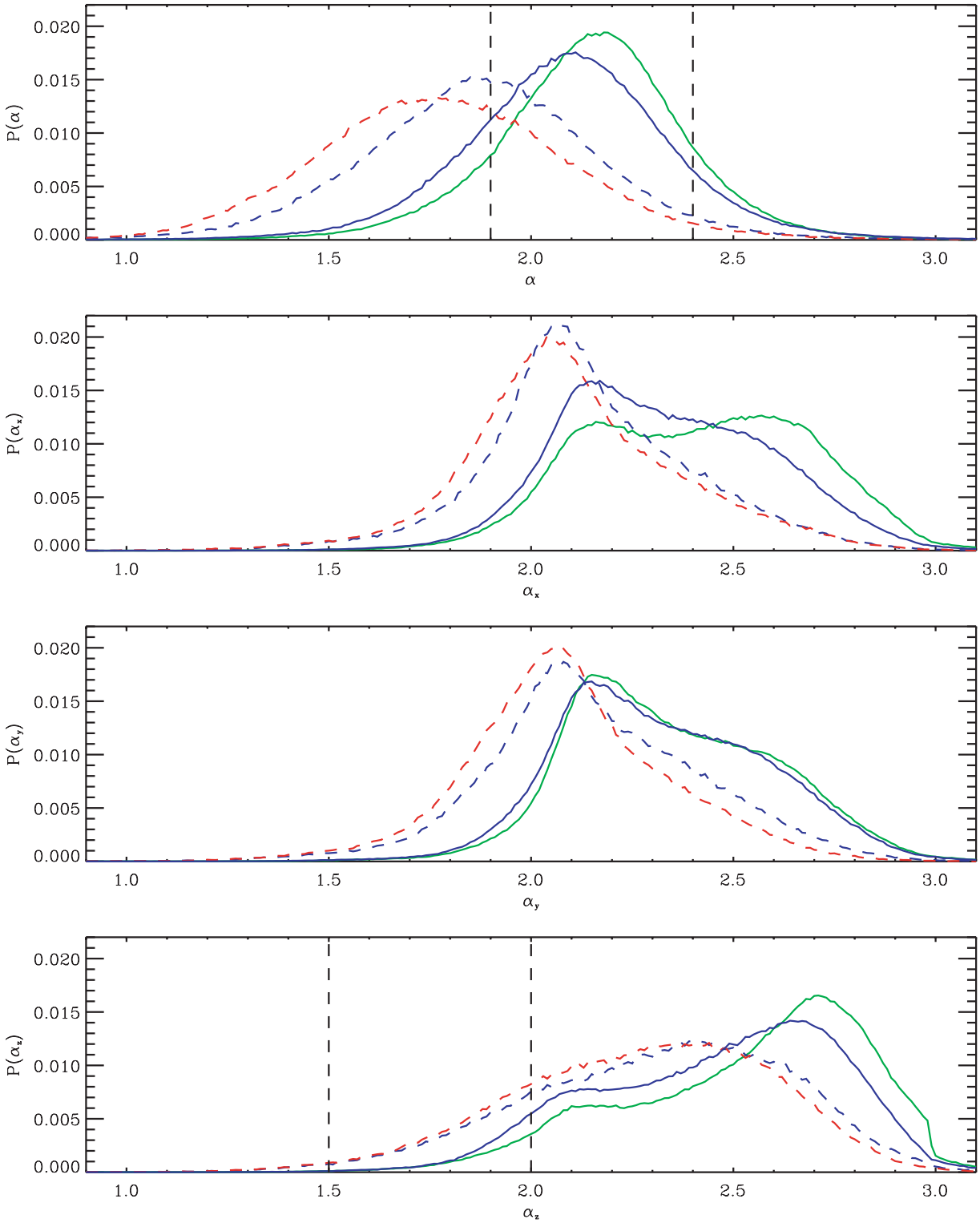

Figure 4. Same as in figure 2 but for the isotropic and anisotropic scaling indices α, α_x, α_y and α_z.

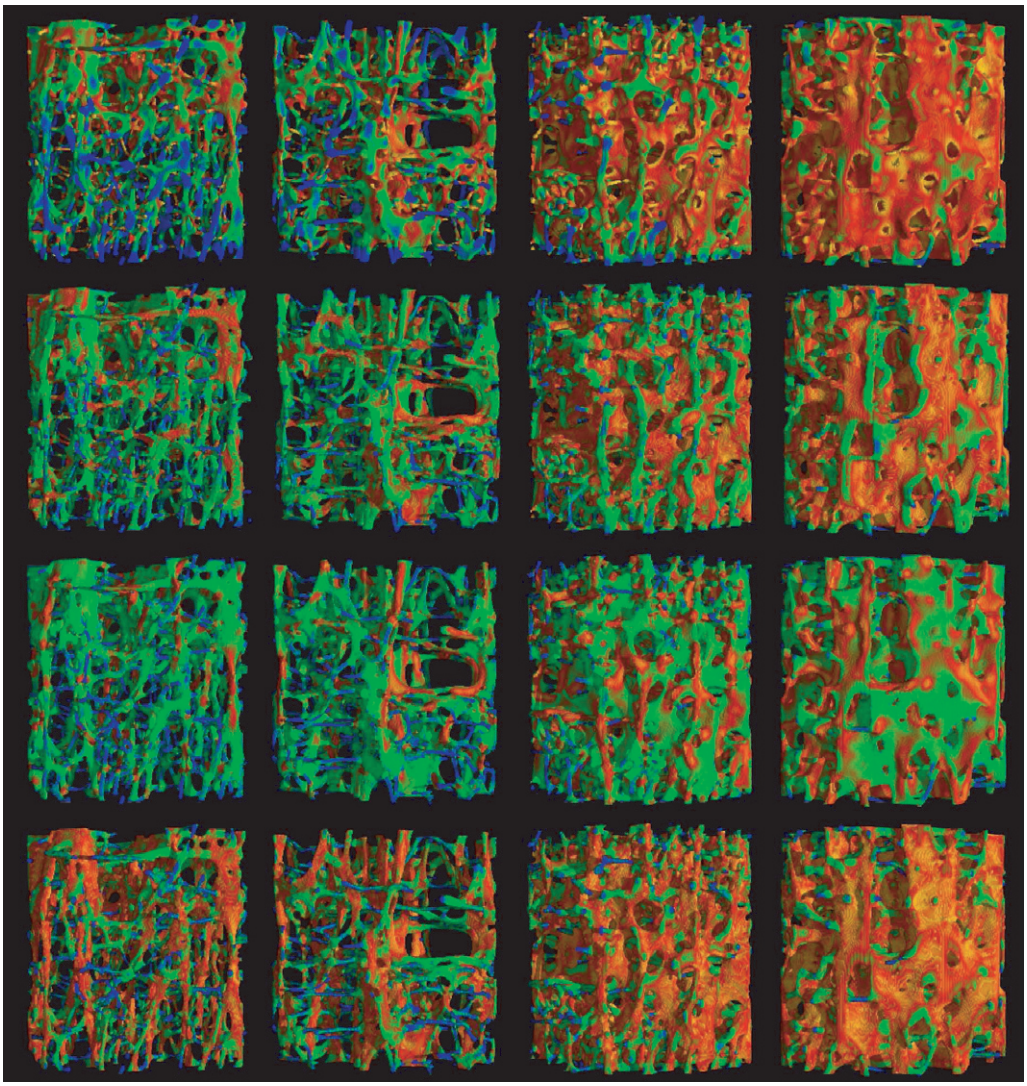

Figure 5. Colour-coded visualization of the isotropic and anisotropic scaling indices for the images shown in figure 1. From top to bottom: α, α_x, α_y and α_z. Note the similarities between α_x and α_y and the differences for α_z. (See stacks.iop.org/NJP/10/125010/mmedia for animations of selected images.)

the anisotropic scaling index along the direction of the external force, α_z, and its probability distribution $P(\alpha_z)$. The spectra peak at higher values $\alpha_z \approx 2.4$–2.7 and have a long tail towards lower values, which becomes larger for weaker bones. These systematic differences in the three spectra for anisotropic scaling indices, which are observed for the whole sample, obviously show the already known fact that there are pronounced anisotropies in the trabecular structure of the vertebrae with significantly more plate-like structural elements aligned along the z-direction.

Given the spectra of the local MFs and scaling indices, we define the texture measures by applying a filtering procedure by taking a window of fixed size and counting the percentage of bone voxels with a value lying within the range of the chosen window. As in previous studies

[5, 43], the fraction of the number of bone voxels lying in the window is defined as an appropriate structure measures $\Delta P(\cdot)$. For this procedure we chose the most promising local measures, namely M_1, M_2, α and α_z. The position and size of the windows are heuristically set to values where the differences in the spectra are expected to be pronounced.

In the first study of this μCT sample we did not perform a rigorous optimization of the window position and window size, nor did we use a two-window technique. Thus we expect our results to improve if more sophisticated texture measures are derived from the spectra of local MFs and scaling indices. The correlations between MCS and the best global measures, i.e. BV/TV $\simeq M_1$ and BS $\simeq M_2$ and the four local measures are shown in figure 6.

In table 2, the correlation coefficients r for the four local measures are listed. We find good correlations for all four measures, where the MF-based measures perform slightly better than the scaling index-based ones. In all four cases we find, however, higher correlations than for the standard histomorphometric measures Tr.N, Tr.Th, Tr.Sp and the SMI. Only BV/TV and BS, which both can be expressed in terms of global MFs, gave similar or better results.

Figure 6 reveals that the variance grows with increasing MCS. To study this effect in detail and to investigate the load dependence of the correlation coefficient we first considered two subsamples, which consisted (a) of the specimens with moderately low MCS, ($60 < \mathrm{MCS} < 120$) and (b) of the weak bone specimens ($\mathrm{MCS} < 60$). Table 3 summarizes the results for subsample (a). We find that for this load regime all structure measures show no or only weak correlations with MCS, indicating that in this transition region from weak to strong bone a clear differentiation based either on bone density or structure measure becomes difficult. A detailed investigation of the possible causes for this unexpected effect is a subject for a future study.

The situation changes, however, when subsample (b) is considered (table 4). Except for the BS we find good correlations for BV/TV as well as for the local structure measures, where it turns out that the scaling index-based measures perform best.

Thus, the structural properties of the trabecular bone become increasingly important for weak, already rarefied bone specimens to assess their stability. This effect is elucidated in more detail in figure 7, in which the correlation coefficients for the various measures are plotted as a function of the cut parameter $\mathrm{MCS}_{\mathrm{cut}}$, which determines the subsample, for which r is calculated. These subsamples consist of a set of specimens satisfying the condition $\mathrm{MCS} < \mathrm{MCS}_{\mathrm{cut}}$.

One can read from the diagram that BV/TV shows a good overall performance with slight decrease for low $\mathrm{MCS}_{\mathrm{cut}}$-values. The second global measure BS, which yields good results for the whole sample, shows the largest decrease for r when considering only weak bones. $\Delta P(M_1)$ and $\Delta P(M_2)$, which both showed better correlations for the whole sample than the scaling index-based measures, also perform significantly worse when $\mathrm{MCS}_{\mathrm{cut}}$ is decreased. $\Delta P(\alpha)$ and $\Delta P(\alpha_z)$ show, on the other hand, a qualitatively different behaviour. In these two cases, the correlations stay roughly constant and even increase yielding maximal values in the range of $60 < \mathrm{MCS}_{\mathrm{cut}} < 80$.

In this regime, a linear combination of the two scaling index-based measures $\Delta P(\alpha)$ and $\Delta P(\alpha_z)$ with BV/TV can also improve the correlation between bone properties and its strength. For the subsample $\mathrm{MCS} < 60$, we obtain $r = 0.65$ for BV/TV and $\Delta P(\alpha)$ and $r = 0.66$ for BV/TV and $\Delta P(\alpha_z)$. It is worth noticing that the combination of BV/TV with the anisotropic scaling index not only gives slightly better results for $\mathrm{MCS}_{\mathrm{cut}} = 60$ than the combination with $\Delta P(\alpha)$, but also yields the highest correlations for the regime $60 < \mathrm{MCS}_{\mathrm{cut}} < 90$, in which most of the specimens lie.

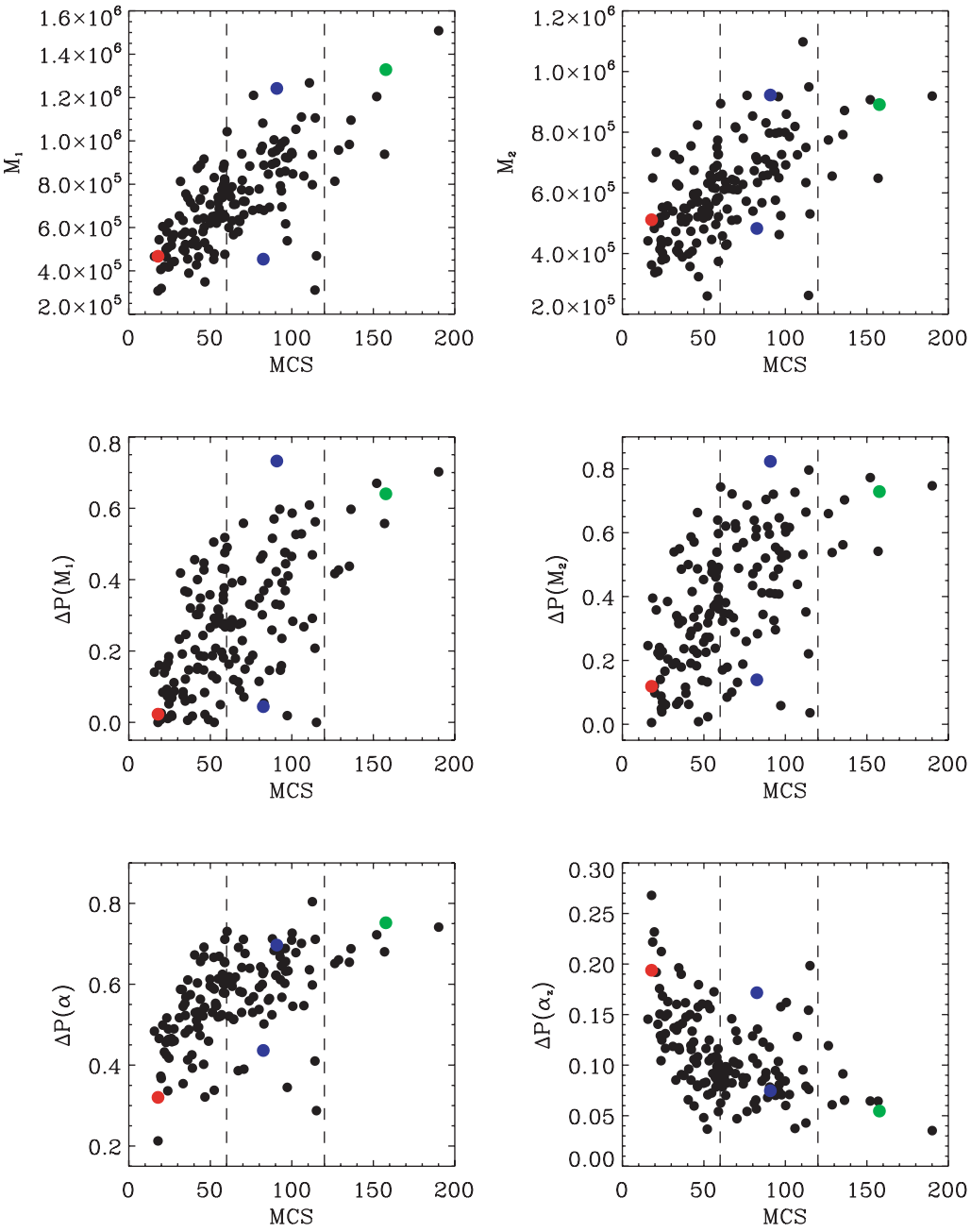

Figure 6. Correlations between MCS and M_1, M_2, $\Delta P(M_1)$, $\Delta P(M_2)$, $\Delta P(\alpha)$ and $\Delta P(\alpha_z)$. The dashed lines indicate the MCS-intervals of the subsamples examined. The coloured filled circles belong to the specimens for which the local MFs, the scaling indices, and the respective probability distributions were shown in more detail in the previous figures.

These results suggest that the scaling indices are not redundant to BV/TV but capture different yet important features of the bone structures for characterizing bone strength. In addition, the alignment of structural components, which is identified by anisotropic texture measures, also plays an important role for the bone stiffness and flexural rigidity.

Table 2. Correlation coefficients r between MCS and the local MFs and isotropic and anisotropic scaling indices calculated for the whole sample.

$\Delta P(M_1)$	$\Delta P(M_2)$	$\Delta P(\alpha)$	$\Delta P(\alpha_z)$
0.61	0.58	0.55	−0.52

Table 3. Correlation coefficients r between MCS and selected structure measures calculated for the subsample with $60 < \mathrm{MCS} < 120$.

BV/TV	BS	$\Delta P(M_1)$	$\Delta P(M_2)$	$\Delta P(\alpha)$	$\Delta P(\alpha_z)$
0.25	0.26	0.30	0.19	0.09	−0.07

Table 4. Correlation coefficients r between MCS and selected structure measures calculated for the subsample with $\mathrm{MCS} < 60$.

BV/TV	BS	$\Delta P(M_1)$	$\Delta P(M_2)$	$\Delta P(\alpha)$	$\Delta P(\alpha_z)$
0.59	0.37	0.54	0.51	0.62	−0.61

5. Conclusions and outlook

In this *in vitro* study, we demonstrated the feasibility of visualizing the 3D complex network of the trabecular bone structure using high resolution μCT imaging techniques and of performing a truly local, i.e. voxel-wise, structure analysis of the isotropic image data. The latter is achieved by calculating local MFs and isotropic and anisotropic scaling indices.

These measures and their corresponding probability distributions reflect well the local structural properties of the trabecular bone and their variations for strong and weak bones. Using anisotropic scaling indices, we could provide evidence for a pronounced alignment of plate- and rod-like structures along the direction of the external force in the vertebrae.

The structure parameters derived from the local measures yield good correlations with the bone strength as measured in mechanical tests. Considering the whole sample the results for the newly defined parameters are better than those obtained for the standard global histomorphometric parameters except BV/TV.

If a subsample consisting only of the weak bones is analysed, the local structural analysis leads to similar and even better correlations with MCS as compared to BV/TV. Thus the textural information becomes increasingly important for weak bones with already rarefied trabecular structure. These findings corroborate the hypothesis that the bone structure and not only its mineral mass is an important ingredient of bone stability.

Besides the already good correlations obtained using the somewhat simple texture measures, a local textural analysis of the trabecular bone offers many other new possibilities for a refined analysis of the inner bone, which will eventually lead to better predictions of disease-related fractures.

Particularly fragile regions of the bone, which lead to higher susceptibility to bone fracture, may be identified by taking the spatial information of the local measures in the definition of the

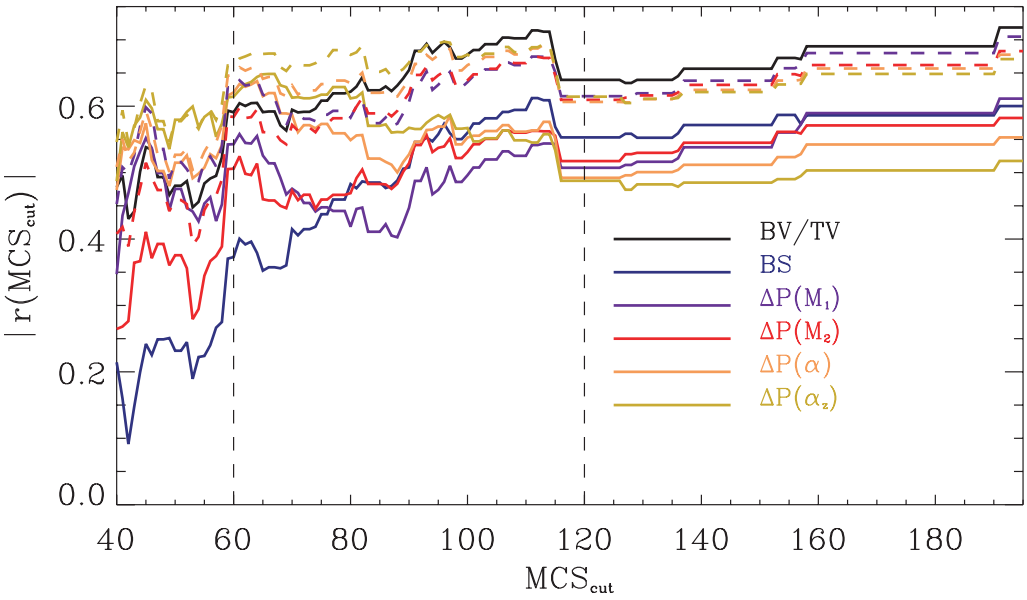

Figure 7. Correlation coefficient as a function of MCS_{cut}. The dashed coloured lines indicate the correlation coefficients, which one obtains when the respective structure measure is combined with BV/TV.

texture measure into account. A combination of the local structural description of the bone with finite element models may lead to a clear identification of those structural elements which are important for the bone strength. In future studies, we will especially investigate these two points mentioned above.

All these analyses may ultimately help to better characterize and thus understand age, disease and drug-induced changes in the trabecular bone structure. Furthermore, one may be able to reveal the effects of pharmaceutical interventions on the inner bone structure beyond simply measuring the BMD.

Acknowledgment

This work is partially supported by the Deutsche Forschungsgemeinschaft (DFG) under the grant MU 2288/2-2.

References

[1] National Institutes of Health 2000 *NIH Consens. Statement* **17** 1–45
[2] Stokstad E 2005 *Science* **308** 1580–1
[3] Chung H, Wehrli F, Williams J and Wehrli S 1995 *J. Bone Miner. Res.* **10** 1452–61
[4] Hildebrand T, Laib A, Müller R, Dequeker J and Rüegsegger P 1999 *J. Bone Miner. Res.* **14** 1167–74
[5] Mueller D, Link T, Monetti R, Bauer J, Boehm H, Seifert-Klauss V, Rummeny E, Morfill G and Räth C 2006 *Osteo. Int.* **17** 1483–93
[6] Link T, Majumdar S, Augat P, Lin J, Newitt D, Lu Y, Lane N and Genant H 1998 *J. Bone Miner. Res.* **13** 1175–82
[7] Räth C, Monetti R, Mueller D, Boehm H, Rummeny E and Link T 2003 *Proc. SPIE* **5032** 1748–56

[8] Baron R 2003 *Primer on the Metabolic Bone Diseases and Disorders of Mineral Metabolism* 5th edn (Washington, DC: ASBMR) pp 1–8
[9] Aubin J, Lian J and Stein G 2006 *Primer on the Metabolic Bone Diseases and Disorders of Mineral Metabolism* 6th edn (Washington, DC: ASBMR) pp 20–9
[10] Ross P 2006 *Primer on the Metabolic Bone Diseases and Disorders of Mineral Metabolism* 6th edn (Washington, DC: ASBMR) pp 30–5
[11] Rubin C and Rubin J 2006 *Primer on the Metabolic Bone Diseases and Disorders of Mineral Metabolism* 6th edn (Washington, DC: ASBMR)) pp 36–41
[12] Huiskes R, Ruimerman R, van Lente G H and Janssen J 2000 *Nature* **405** 704–6
[13] Wolff J 1892 *Das Gesetz der Transformation der Knochen* (Berlin: Hirschwald)
[14] Michielsen K and De Raedt H 2001 *Phys. Rep.* **347** 461–538
[15] Räth C, Bunk W, Huber M, Morfill G, Retzlaff J and Schuecker P 2002 *Mon. Not. R. Astron. Soc.* **337** 413–21
[16] Räth C, Schuecker P and Banday A 2007 *Mon. Not. R. Astron. Soc.* **380** 466–78
[17] Hildebrand T and Rüegsegger P 1997 *Comput. Methods Biomech. Biomed. Eng.* **1** 15–23
[18] Mecke K, Buchert T and Wagner H 1994 *Astron. Astrophys.* **288** 697–704
[19] Kerscher M, Schmalzing J, Retzlaff J, Borgani S, Buchert T, Gottlöber S, Müller V, Plionis M and Wagner H 1997 *Mon. Not. R. Astron. Soc.* **284** 73
[20] Kerscher M, Schmalzing J, Buchert T and Wagner H 1998 *Astron. Astrophys.* **333** 1
[21] Sahni V, Sathyaprakash B S and Shandarin S F 1998 *Astrophys. J. Lett.* **459** 5
[22] Schmalzing J, Buchert T, Melott A L, Sahni V, Sathyaprakash B S and Shandarin S F 1999 *Astrophys. J.* **526** 568
[23] Hikage C, Schmalzing J, Buchert T, Suto Y, Kayo I, Taruya A, Vogeley M, Hoyle F, Gott J and Brinkmann J 2003 *Publ. Astron. Soc. Japan* **55** 911–31
[24] Hikage C, Coles P, Grossi M, Moscardini L, Dolag K, Branchini E and Matarrese S 2008 *Mon. Not. R. Astron. Soc.* **385** 1613–20
[25] Schmalzing J and Gorski K 1998 *Mon. Not. R. Astron. Soc.* **297** 355
[26] Komatsu E *et al* 2003 *Astrophys. J. Suppl.* **148** 119–34
[27] Eriksen H, Novikov D, Lilje P, Banday A and Gorski K 2004 *Astrophys. J.* **612** 64–80
[28] Komatsu E *et al* 2008 arXiv:0803.0547
[29] Mecke K and Sofonea V 1997 *Phys. Rev.* D **56** R3761
[30] Mecke K 1996 *Phys. Rev.* D **53** 4794
[31] Santalo L 1976 *Integral Geometry and Geometric Probability* (Reading, MA: Addison-Wesley)
[32] Stoyan D, Kendall W and Mecke J 1989 *Stochastic Geometry and its Applications* (Berlin: Akademie Verlag)
[33] Hadwiger H 1957 *Vorlesungen über Inhalt, Oberfläche und Isoperimetrie* (Berlin: Springer)
[34] Boehm H, Link T, Monetti R, Mueller D, Rummeny E, Newitt D, Majumdar S and Räth C 2004 *Proc. SPIE* **5370** 172
[35] Boehm H, Link T, Monetti R, Kuhn V, Eckstein F, Räth C and Reiser M 2006 *Proc. SPIE* **6144** 61446X
[36] Grassberger P and Procaccia I 1983 *Phys. Rev. Lett.* **50** 346–9
[37] Farmer D, Ott E and Yorke J 1983 *Physica* D **7** 153–80
[38] Grassberger P, Badii R and Politi A 1988 *J. Stat. Phys.* **51** 135–78
[39] Räth C and Morfill G 1997 *J. Opt. Soc. Am.* A **14** 3208–15
[40] Monetti R, Boehm H, Mueller D, Rummeny E, Link T and Räth C 2004 *Proc. SPIE* **5370** 215–24
[41] Sauer T, Yorke J and Casdagli M 1991 *J. Stat. Phys.* **65** 579–616
[42] Ivlev A *et al* 2000 *Phys. Rev. Lett.* **100** 095003
[43] Boehm H, Räth C, Monetti R, Mueller D, Newitt D, Majumdar S, Rummeny E, Morfill G and Link T 2003 *Invest. Radiol.* **38** 269–80